Highly Efficient On-surface Synthesis of Fused N-heterocyclic derivatives

Bruno de la Torre

bruno.de@upol.cz

  Palacky University   https://orcid.org/0000-0002-6462-6833

Alejandro Jiménez-Martín

  Palack&#x00FD   https://orcid.org/0000-0002-4956-4996

Tatiana Munteanu

  Aix Marseille Univ

Qifan Chen

  FZU

Simon Pascal

  Aix Marseille Univ   https://orcid.org/0000-0001-8387-494X

Benjamin Mallada

  Regional Centre of Advanced Technologies and Materials   https://orcid.org/0000-0002-8209-9977

Pingo Mutombo

  Institute of Physics of the Czech Academy of Science   https://orcid.org/0000-0002-8175-7587

Olivier Siri

  Aix Marseille Univ, CNRS, CINaM

Pavel Jelinek

  Czech Academy of Sciences   https://orcid.org/0000-0002-5645-8542

Article

Keywords:

Additional Declarations: There is **NO** Competing Interest.

Abstract

The synthesis of N-fused heterocycles is a crucial element in organic chemistry. However, it involves multiple steps that add complexity and reduce overall yields. Here, we introduce the high-yield on-surface synthesis of N-heterocyclic compounds employing the intramolecular hydroamination of alkyne-functionalized molecular precursors under mild thermal conditions in an ultra-high vacuum environment on an Au(111) surface. This method offers an efficient preparation of two discrete N-heterocyclic derivatives using a single gold(0)-atom catalyst. Notably, the synthesis introduces two pyrrole groups into quinoidal-based precursor, enabling the formation of two fused pyrrolo-benzoquinonediimine compounds with tailored electronic band-gap not achievable in solution chemistry. To analyze the resulting reaction products, we utilized scanning tunneling microscopy and non-contact atomic force microscopy with single bond resolution, comparing these products to those obtained through traditional solution methods. We further performed computational studies to elucidate detailed mechanistic insights into the on-surface reaction course.

Introduction

N-fused heterocycles are ubiquitous within critical molecules, including biologically active natural and synthetic compounds and fine chemicals for use in functional materials. Particularly, five-membered N-heterocyclic compounds are an important class of heterocyclic compounds that are found frequently in various bioactive molecules and natural products.[1] Conversely, synthesizing N-fused heterocycles typically requires multiple steps, introducing complexity and labor intensity to the overall process. Attaining high yields at each synthesis step poses a challenge, with potential issues such as side reactions, incomplete reactions, and purification difficulties contributing to reduced overall yields.[2] In the realm of organic synthesis, the intramolecular hydroamination/cyclization (IHC) reaction of alkynes represents a versatile and robust strategy for crafting multifunctional N-heterocycles in solution-chemistry.[3−6]

The traditional hydroamination reaction, involving the activation of $C \equiv C$ triple bonds in precursor molecules containing alkynes for the subsequent addition of heteroatomic nucleophiles, has been associated with substantial activation energy barriers and requires the use of costly transition metal catalysts. Recent advancements in metal-catalyzed heterocycle construction have introduced a more effective approach.[7−11] In this context, gold complexes, at different oxidation state, have emerged as highly effective catalysts for the electrophilic activation of alkynes, enabling nucleophilic additions to proceed under mild reaction conditions.[12] Notably, these gold catalysts selectively activate π-bonds of alkynes, facilitating the attack of various nucleophiles. Specifically, Au(I)-catalyzed hydroamination reactions have yielded notable success in formally adding N − H reagents onto triple bonds in both intermolecular[13,14] and intramolecular[15] contexts. Yet, hydroamination presents a considerable challenge because of the repulsion between a nitrogen lone pair and the alkyne π-system, and simultaneously poses difficulty in controlling the regioselectivity, which consequently limits the reaction yield.[1] Given the

significant value attributed to N-fused heterocycles, there is a compelling need for explorations into novel and more efficient synthetic methodologies.[16,17]

Inspired by well-established in-solution methodologies, on-surface synthesis has recently emerged as a remarkably effective method for achieving precise atomic-level fabrication of molecular structures mimicking known in-solution protocols.[18–21] This approach can be seen as an extension of heterogeneous catalysis, where the initial precursors, intermediate states, and reaction products all exist in an adsorbed state, typically under ultra-high vacuum conditions. Notably, its combination with scanning probe microscopy enables meticulous molecule-by-molecule characterization with single-bond precision[22,23] and isomer discrimination.[24] Recent advancements in on-surface synthesis have introduced innovative synthetic approaches that can rarely be achieved by conventional chemical means.[25–28] Despite that, examples of on-surface IHC reactions are missing. Furthermore, there is a critical need for a comprehensive comparative analysis between traditional and on-surface chemistry. Such an analysis is essential to provide insights that could broaden the current range of synthetic protocols and enhance our understanding of fundamental reaction mechanisms.

In this study, we provide an innovative approach for the highly efficient synthesis of N-heterocyclic compounds *via* hydroamination and subsequent cyclization on Au(111) substrates and compare with that obtained by traditional methods in solution-phase chemistry. The precursor, 2,5-diamino-1,4-benzoquinonediimines (1, 3), featuring a central quinoidal ring with two alkyne moieties and two amine functions, appears to be prime candidates for tandem hydroamination reactions of the alkynes, followed by cyclization under mild conditions (Scheme 1). In solution-phase chemistry, the activation of the alkyne unit by Au(III) results in the moderate-yield formation of the monocyclized compound **2**. On the surface, the presence of single Au(0) adatoms nearby facilitates low-energy hydrogen migration from the amino group to the C≡C triple bond. This process evolves into fused N-heterocyclic compounds through an intramolecular cyclization reaction, leading to the high-yield production of compounds **4** and **5**. Leveraging scanning tunneling microscopy (STM) and advanced bond-resolved non-contact atomic force microscopy (nc-AFM),[29] we effectively discerned the molecular configurations of reaction products formed on surfaces, unambiguously determining their structural changes. The reaction mechanism was further evaluated through density functional theory (DFT) and molecular mechanic (MM) calculations, rationalizing the occurrence of the final products.

Results

Precursors **1**, **3** belong to a distinctive class of compounds characterized by a unique distribution of their π-electrons. Their molecular structure contains 12 π-electrons indeed, but the molecule is best described as constituted of two independent π-subsystems containing 6 conjugated π-electrons (the nitrogen lone pair is conjugated with the two double bonds), chemically linked via two C-C σ-bonds, but electronically not conjugated.[30–32] As a result, a peculiar reactivity can be expected through intramolecular hydroamination cyclization.

We first synthesized **1** in 65% yield by using a protocol adapted from literature procedures[12,33,34] with a supplementary oxidation step before the final purification. Next, we envisaged from **3** the gold-catalyzed IHC by using HAuCl$_4$•3H$_2$O (0.3 equiv.). Interestingly, only one subunit of the molecule reacted, leading to the formation of **2** in 54% yield incorporating a single pyrrole unit. The ^{1}H NMR spectrum of **2** revealed an asymmetric molecule with a pyrrolic C-H proton at 6.63 ppm. ^{13}C NMR confirmed single cyclization, retaining the C $\equiv$ C triple bond at 99 and 105 ppm and a correlation peak could be observed in ^{1}H-^{13}C HSQC spectrum corresponding to an olefinic CH (δ_C = 11.8 ppm; δ_H = 6.63 ppm). As expected for **2**, ^{1}H NOESY indicated spatial correlation between the indole ring's CH and Si^{i}Pr$_3$ protons (Figures S17 and S18). High-resolution mass spectrometry of **2** validated the monocyclization, showing a peak at m/z = 497.3490 Da corresponding to C$_{28}$H$_{49}$N$_4$Si$_2{}^+$ species (see more in the supplementary information).

Finally, the structure of **2** was fully established by X-ray diffraction studies that clearly confirmed the formation of a fused pyrrolo-benzoquinonediimine derivative incorporating the C $\equiv$ C triple bond (Fig. 1b and Figure S1). Further examination of the bond distances of **2** does not show the expected bond equalization for an aromatic pyrrole. This observation can be explained by the fused pyrrolo-benzoquinonediimine arrangement, in which the shared carbon-carbon bond functions as a C = C double bond, preserving the conjugation (rather than delocalization) of the π system within the benzoquinonediimine unit. These characteristics account for the absence of double cyclization in molecule **2** that can be rationalized by the nature of the catalyst. In fact, HAuCl$_4$ is an anionic gold complex with an H$^+$ counterion, which might participate in an acid-base reaction (protonation of an imine function in **1**) to generate the stabilized cationic species **6**, as depicted in Fig. 1a. This diminishes the nucleophilic character of the NH$_2$ function, thereby decreasing reactivity. To validate this, we sought to synthesize biscyclized molecule **7** from monocyclized **2** under identical conditions (same catalyst), resulting in the complete recovery of the precursor. This underscores the influence of a "parasitic" acid-base reaction in our study.

Next, we envisaged the reaction on gold surface from the closely related analogue **3** for which the absence of a sterically bulky group should enable strong interaction with the substrate. As illustrated in Fig. 2, a series of STM images carefully assessed the molecular landscape existing within the submonolayer regime, revealing the stable organization of precursors into distinctive two-dimensional islands (Fig. 2a). Subsequent elevation of the temperature of the Au-covered surface to approximately 370 K initiated a pivotal thermal transformation of the precursor, leading to the emergence of distinctly different molecular products, as captured in the visually striking depiction provided in Fig. 2b. The STM image post-annealing at roughly T = 370 K offered a vivid portrayal of the dynamic chemical transformation undergone by the precursor and its subsequent self-assembly. Prominently visible in the STM images were the planar structures of the resulting products, distinctly forming one-dimensional chains guided by the intricate herringbone reconstruction adorning the surface. These molecular chains consist of two distinct molecular products, designated as type A (yield 79%) and type B (yield 21%) (see

methods for calculation of yield in the SI), easily identifiable by their characteristic elongated and boomerang-like shapes, respectively (see Fig. 2c, g).

To determine unambiguously the chemical structure of the molecular backbone of the final products, we employed high-resolution nc-AFM imaging supported by theoretical calculations. Figures 2d and h display high-resolution nc-AFM images acquired with CO-functionalized tips of type A and B chains comprising products **4** and **5**, respectively. We performed a series of nc-AFM simulations using fully optimized molecular structures obtained by the total energy DFT calculations of possible chemical conformations of type A and B. Figure S2 displays simulated nc-AFM images of the considered structures. Based on agreement with experimental observations, we can rule out the presence of covalently bonded chains of type A and B. In the case of a type A chain, based on asymmetric contrast on heterocycles containing nitrogen atoms, we can confirm the presence of the pyrrole group. Figures 2d and e compare the experimental and simulated AFM images that show excellent agreement, which enables us to determine that type A chain consists of product **4**, as depicted in Fig. 2f. Moreover, we should note that this configuration of type A also has the lowest total energy between all considered structures, optimizing the strength of the dispersive and electrostatic intermolecular interactions (see Figures S2 and S3).

However, in the case of the B-type chain, the situation is not so clear-cut, because different variants of the arrangement of hydrogen on the molecular backbone give a very good agreement with the contrast of the experimental nc-AFM image, see Figures S2d-f. Thus, we cannot determine the chemical structure unequivocally based on the comparison of the experimental and the simulated nc-AFM images. Nevertheless, according to the total energy calculation of free-standing chains of type B, the most thermodynamically stable variant is the chain formed by product **5**, as shown in Figure S2. The high-resolution nc-AFM images enable us to identify the supramolecular arrangement of both types of chains. While the type A chain formed by molecule **4** adopted a truncated configuration, molecule **5** organizes itself in a head-to-tail arrangement, culminating in chains characterized by specific intermolecular distances measuring 7.51 (± 0.05) Å and 7.39 (± 0.05) Å, respectively. Remarkably, we discovered that the molecular chains can be manipulated effortlessly by inducing lateral displacements with the STM tip (see Figure S4). It was observed that segments containing **5** could be easily displaced, with the molecules moving collectively while preserving their chain configuration. This investigation serves to probe the chemical stability of the hydrogen-bonded molecular chains. An in-depth analysis of consecutive sequences of **4** and **5** molecules revealed the presence of four hydrogen bonds per molecule. The shape, whether linear or truncated, of the resulting chain was determined by the symmetric or antisymmetric configuration of the pyrrole moieties inherent in molecules **5** and **4**.

We observed that the precise positioning of pyrrole units significantly influences not only the molecular arrangement but also the electronic structure of the molecules. In Fig. 3a, constant-current *dI/dV* spectra are presented, acquired over the edge of a chain containing molecules **4**, with the substrate spectra provided for reference. The *dI/dV* spectra reveal two distinct peaks at -1.9 and 2.0 eV, corresponding to HOMO and LUMO (where HOMO and LUMO represent the highest occupied and lowest unoccupied molecular orbitals, respectively), establishing a HOMO-LUMO gap of approximately 3.9 eV. The calculated

DFT-PBE0 gap of ~ 3.7 eV for the free-standing **4** product aligns well with the experimental findings. Subsequently, spatially resolved scanning tunneling spectroscopy of HOMO reveals dot-like states over outer carbon at the indole units (Fig. 3a). The *dI/dV* map of the LUMO displays states located over nitrogen sites of the molecule.

The DFT-calculated *dI/dV* map of the canonical HOMO and LUMO of **4** (depicted in Fig. 3b, c) closely aligns with the experimental observation. In comparison, the calculated electronic gap for the free-standing **5** distinctly indicates electronic structure renormalization, with a shift of the HOMO closer to the Fermi level of the metal by approximately 1 eV, thus lowering the molecular gap of ~ 3 eV (see Figure S5). Calculated maps of the HOMO reveal enhancements in conductance closely symmetrically located over outer carbon at the indole units, while the LUMO is situated around the imine units. Unfortunately, the high mobility of **5** on Au(111) surface prevented the extraction of such information from the experiments.

Certainly, on-surface hydroamination reactions illustrate noticeable differences compared to the traditional synthesis in solution-phase. Specifically, the on-surface synthesis reveals a high yield with no evident side reactions beyond the de-hydrogenated **5** molecular structures (Figure S6) compared to the moderate yield achieved in solution. Moreover, the on-surface reaction facilitates the complete cyclization of both alkynes, forming two pyrrole moieties per molecule. Conversely, in solution, only one pyrrole unit was detected per molecule. In solution, the hydroamination reaction is generally driven by Au(I)/Au(III)-based catalysis. However, on the surface at elevated temperatures, there is an abundant amount of diffusing single gold atoms, so-called adatoms.[35,36] These gold adatoms have a neutral charge due to the presence of a gold surface underneath. Moreover, it has been recently demonstrated that these Au(0) adatoms may steer on-surface reactions.[28,37−39]

These findings strongly suggest a deviation from the conventional nucleophilic attack of the terminal alkyne,[41,42] indicating an alternative mechanism on the surface. Furthermore, the two-dimensional constraint imposed by the surface impacts the behavior of individual gold adatoms and reactants, respectively, confining their movement. Subsequent theoretical analysis will delve into the reaction pathways leading to forming **4** and **5** on the surface and the notable disparity in the yield obtained for each.

To get more insight into the on-surface reaction mechanism, we carried out free-energy QM/MM simulations exploring different reaction pathways. Figure 4 displays the optimal reaction pathways from precursor **3** towards products **4** and **5** according to our QM/MM simulations. These reaction schemes encompass hydrogen migration in tandem with the annulation or cyclization processes of both alkynes divided into two successive steps. Next, we will describe in detail each step of the reaction mechanism as well as the origin of different yields of products **4** and **5**.

Firstly, three distinct rotamers of the precursor, namely **IS1**, **IS2**, and **IS3**, were initially identified, with **IS2** being the most stable according to free-standing DFT calculations optimizing steric strain and electrostatic interaction between nitrogen lone pairs and hydrogen atoms (see Figure S7). However, the

situation on the surface provides a different scenario. The presence of Au(0) adatoms at RT, electrostatically attracted by the nitrogen lone pair, results in an average increase in the stability of **IS4** by about 0.35 eV concerning the **IS3** (see Figure S8). Consequently, this rotamer becomes the most populated, assuming its dominant role in the reaction course. Figure 4a shows the initial phase that entails the migration of a single hydrogen atom from the amine moiety to the central carbon of the terminal alkyne, leading to **IM1**. A single Au(0) adatom nearby plays a key role in this transfer, reducing the energy barrier from 2.78 eV to 1.48 eV compared to the reaction without Au adatoms (as depicted in Figure S9). In contrast to our findings, dehydrogenation of the terminal alkyne typically results in the manifestation of Glaser-like coupling. This phenomenon has, indeed, been documented on Au(111)[43] under higher temperature conditions and on surfaces characterized by increased reactivity, such as Ag(111)[44,45] and Cu(111).[43] Similarly, other competing dehydrogenation processes of the alkyne group, as well as hydrogen transfer within the alkyne group assisted by a single Au adatom, shown in Figure S10, have a much larger activation barrier compared to the hydrogen transfer from the amine to central carbon atoms of the alkyne segment. This modification renders the process more thermodynamically feasible at the experimentally relevant temperatures.

This primary step carries significant importance in unraveling the reaction mechanism. A detailed analysis of this reaction step reveals that the proximity of the Au adatom weakens the triple carbon bond on alkyne, as indicated by our bond length analysis (Figure S11). This prompts a redistribution of charge, triggering the transfer of a hydrogen atom from the NH_2 to the central carbon through a sigmatropic reaction, culminating in forming a sp^3 carbon (**IM1**). It is important to note that this process differs from the well-established mechanism in solvents where the Au(I) attacks the central terminal alkyne, forming a new bond between the nucleophile and the carbocation. The efficacy of the metal catalysts in the hydroamination/cyclization in solution substantiates the involvement of a reaction pathway wherein the C-C bond coordinates with the nucleophilic metal. Without this coordination, the amino group cannot effectively attack the alkyne carbon bonded to the phenyl group due to the molecular rigidity that inhibits bending. The coordination of $C \equiv C$ to a metal induces a decrease in the bond angles at the alkyne carbons, thereby facilitating the accessibility for the amino group to attack the alkyne carbon.[46] This first transformation serves as a pivotal precursor for understanding the subsequent steps of the reaction. It is succeeded by a cyclization process, resulting in the formation of the primary pyrrole moiety, leading to **IM2**, a common intermediate state for both **4** and **5**.

The critical step determining the formation of either product **4** or **5** entails hydrogenation and cyclization processes of the second terminal alkyne, involving the amino group (refer to Fig. 4c, d). At this bifurcation point, the positioning of the surrounding Au(0) adatom leads to different ground states (**IS's**). Figure 4b shows that **IS'1**, being 0.58 eV more favorable than the next one (**IS'3**), emerges as the leading state considered for further analysis. Similar to the formation of the first pyrrole, the ground state **IS'1** is followed by a sigmatropic adatom-mediated hydrogen transfer from the NH_2 amino group towards the central carbon alkyne (**IM3**) and a subsequent cyclization reaction at the para position, leading to the

formation of **4** with low energy barriers reachable with the mild conditions of the experiment, as depicted in Fig. 4c.

The formation of **5** requires a unique starting point to enable the cyclization reaction directed toward the ortho position (Fig. 4d). Its notably lower yield compared to **4** implies a less likely reaction path for **5**. Hence, our focus shifts to **IS's** states with elevated energy. Among **IS'2**, **IS'3** and **IS'4**, the former stands out, showing lower energy barriers, thus considered for further analysis. Proceeding from **IS'2**, the reaction closely mirrors **IS'1**, where Au(0) adatom mediates hydrogenation of the central alkyne, leading to the **IM4** state. This state marginally differs from **IM3** in the Au adatom's position and relative hydrogen conformations. At the subsequent stage, two channels appear, describing the pyrrole construction at the *para* or *ortho* sites for **5**. The straightforward cyclization process yields **4** with an energy barrier of 1.16 eV (see Figure S12). However, an alternate channel emerges with a lower energy barrier (0.47 eV) involving the alkyne group's rotation guided by the gold adatom, leading to **IM5** and subsequent cycling toward the ortho position with an energy barrier of 0.69 eV. Despite identifying other potential reaction pathways, this one is favored by approximately 0.24 eV (see Figure S12). The identified energy barrier giving rise to both products provides a route for the selection of a pure (only **4**) or mixed (**4** and **5**) sample by fine-tuning the thermal energy reservoir. Notably, the second pyrrole's formation in both **4** and **5** occurs on the surface, with no evidence of this second cyclization found in the solution, highlighting the potent capabilities of on-surface synthesis in achieving high-yield, low-energy hydroamination reactions beyond the scope of traditional chemistry. Furthermore, many initial hydroamination reactions, as per early reports, necessitate the utilization of toxic reagents and severe conditions, including high temperature or high dilution, which do not align with the principles of green chemistry.[47,48]

Conclusions

Highly efficient synthesis of N-heterocyclic derivatives was successfully achieved through a tandem intramolecular hydroamination/cyclization reaction involving alkyne moieties and amine groups. This process was observed on both Au(111) substrate and in solution but we have clearly demonstrated that the reaction is largely favored on the surface due to a different mechanism inherent in the presence of the gold surface. The subsequent reaction, taking place on the surface, results in high-quality products through a cascade hydroamination/cyclization process. This process introduces two cis-, trans-pyrrole groups into the precursor backbone, significantly influencing the electronic structure of the products. These transformations were directly observed through STM/nc-AFM. DFT calculations have verified the energetically favored cis-cyclization scenario, attributed to the influence of a single Au(0) adatom nearby, resulting in a highly efficient production. On-surface synthesis of N-heterocyclic compounds may promote the fabrication of various types of integral components in biologically active molecules, drugs, and pure chemical.

Methods

Experimental methods

Experiments were conducted in a custom-build scanning tunneling microscope (STM)/non-contact atomic force microscope (nc-AFM) system (CreaTec Fischer & Co. GmbH) in an ultra-high vacuum (UHV) environment with a base pressure below 5 x 10^{-10} mbar hosting a low temperature (4.2 K) cryostat. The Au(111) substrate was prepared by standard cycles of Ar^+ sputtering and annealing at 800 K. Images were acquired with a Pt/Ir tip attached to a qPlus sensor[49] (resonant frequency $\approx$ 30 kHz; stiffness $\approx$ 1800 N m^{-1}; Q $\approx$ 70k) by applying a bias voltage to the sample. For nc-AFM imaging, we used a frequency modulation method by keeping the oscillation amplitude constant at 50 pm. Sharp metallic tips were obtained by gentle indentations on the bare surface. For AFM imaging, a single CO molecule was picked up by the tip-apex after dosing on the cold sample. The images were analyzed with the WSxM software.[50]

The molecular precursor **3** was outgassed in UHV for several hours and then thermally sublimated in UHV onto the clean Au(111) substrate kept at room temperature from a tantalum crucible maintained at 120 ºC. After annealing step at 100 ºC, the sample was transferred to the STM stage held at 4.2 K for further characterization.

Theoretical methods

For the QM/MM simulations we have employed the Fireball/AMBER software.[51] The classical part is the metal surface, and to define its forces we employ the interface force-field, whereas the quantum region, consisting of the molecule and one gold adatom, is treated at the BLYP-DFT level with the Fireball software,[52] a local-orbital DFT code which employs an optimized basis set of pseudo-atomic orbitals. The forces thus obtained are then managed by AMBER and integrated to derive the dynamics.[53] We have employed a combination of Umbrella Sampling Simulations (US) and Steered Molecular Dynamics (SMD) to unveil the features of the reaction mechanism and calculate the free energy profiles of the reactions.[54–56] Before the US or SMD, we have performed a QM/MM geometry optimization followed by a thermalization under 300 K to stabilize the system. We use the Langevin thermostat as implemented in AMBER to simulate the canonical ensemble.[57] We use the Alan Grossfield´s implementation for the Weighted Histogram Analysis Method (WHAM)[58] to calculate free energy profiles associated to each reaction from the US. On each of these cases, an initial SMD is employed to drag the corresponding reaction coordinate and generate structures which can be used as seeds for each US window.

We performed Density Functional Theory calculations as implemented in the FHI-aims code[59] in order to obtain the electronic properties of all the free-standing molecules. First, they were thoroughly relaxed using the hybrid functional B3LYP (Becke, 3-parameter, Lee−Yang-Parr)[60,61] to get an optimized structure. Then, they were linked together to form one-dimensional chains following the models derived from the experimental findings. These chains were again relaxed to optimize their lattice constants. Note that all the calculations were performed using the Tkachenko-Scheffler treatment of the van der Waals

interactions.[62] The structural optimization was stopped when the remaining atomic forces and the total energy were found below 10^{-5} eV and 10^{-2} eV/Å and respectively. A Monkhorst-Pack grid of 1x18x1 was used for the integration of the Brillouin zone.

AFM image simulations were carried up using the ProbeParticle code[63,64] that takes into account the electrostatic and the van der Waals (vdW) between the CO tip and the surface. The DFT densities were used to determine the Pauli repulsion and the van de Waals interactions. The electrostatic forces were calculated from the Hartree potential obtained from DFT calculations. All the simulations were performed with a lateral stiffness of (k) = 0.25 N/m.

We simulated *dI/dV* maps using the PP-STM code[65] with an CO rigid tip. The eigenstates needed for the simulations of the one-dimensional chain bands were calculated with the Fhi-aims code. The *dI/dV* figures were obtained at characteristic energy positions corresponding to the valence and conduction bands respectively. We set the Lorentzian width parameter for broadening of the eigenstates to 5 meV.

Declarations

Data availability

Source data are provided with this paper. The data supporting this study's findings are also available from the authors on request and in the repository. https://…

Author Contributions Statement

P.J., O.S. and B.T. conceived and designed the experiments. P.J., O.S. and B.T. supervised the project and led the collabo-ration efforts. A.J.-M., B.M. and B.T. carried out the SPM experiments, obtained the data and performed on-surface reactions. T.M, S.P. and O.S. synthesized the precursors and carried out the reactions in solution. A.T. performed all the NMR experiments in solution. The experimental data were analyzed by A.J.-M. and B.T.; and discussed by all the au-thors. Q.C., P.M. and P.J. performed the theoretical calcula-tions. The manuscript was written by A.J.-M., P.J., O.S. and B.T. with contributions from all the authors.

Competing Interests Statement

The authors declare no competing interests.

References

1. Eftekhari-Sis, B., Zirak, M.& Akbari, A. Arylglyoxals in Synthesis of Heterocyclic Compounds. *Chem. Rev.* **113**, 2958–3043(2013).

2. Eicher, T., Hauptmann, S. & Speicher, A. The Chemistry of Heterocycles: Structures, Reactions, Synthesis, and Applications, Wiley-VCH, (2012).

3. Beller, M., Seayad, J., Tillack, A.& Jiao, H. Catalytic Markovnikov and Anti-Markovnikov Functionalization of Alkenes and Alkynes: Recent Developments and Trends. *Angewandte Chemie International Edition* **43**, 3368–3398(2024).

4. Hartwig, J. F. Raising the Bar for the "Perfect Reaction." *Science* **297**, 1653–1654(2002).

5. Togni, A. *Catalytic Heterofunctionalization* (pp. 1-276). H. Grützmacher (Ed.). Weinheim: Wiley-VCH (2001).

6. Patel, M., Saunthwal, R. K. & Verma, A. K. Base-Mediated Hydroamination of Alkynes. *Acc. Chem. Res.* **50**, 240–254 (2017).

7. Huang, L., Arndt, M., Gooßen, K., Heydt, H. & Gooßen, L. J. Late Transition Metal-Catalyzed Hydroamination and Hydroamidation. *Chem. Rev.* **115**, 2596–2697 (2015).

8. Müller, T. E., Hultzsch, K. C., Yus, M., Foubelo, F. & Tada, M. Hydroamination: Direct Addition of Amines to Alkenes and Alkynes. *Chem. Rev.* **108**, 3795–3892 (2008).

9. Sengupta, M.; Das, S.; Islam, Sk. M.; Bordoloi, A. Heterogeneously Catalysed Hydroamination. *Chem. Cat. Chem.* **13**, 1089–1104 (2021).

10. Clentsmith, G. K. B., Field, L. D., Messerle, B. A., Shasha, A. & Turner, P. Intramolecular Cyclization of Ortho-Alkynylanilines by Rh(I)-Catalyzed Hydroamination to Yield Benzo(Dipyrroles). *Tetrahedron Letters* **50**, 1469–1471 (2009).

11. Krüger (née Alex), K., Tillack, A. & Beller, M. Catalytic Synthesis of Indoles from Alkynes. *Advanced Synthesis & Catalysis* **350**, 2153–2167 (2008).

12. Dorel, R. & Echavarren, A. M. Gold(I)-Catalyzed Activation of Alkynes for the Construction of Molecular Complexity. *Chem. Rev.* **115**, 9028–9072 (2015).

13. Uchimoto, K., Fukuda, Y., Utimoto, K. & Nozaki, H. Preparation of 2,3,4,5-Tetrahydropyridines from 5-Alkynylamines under the Catalytic Action of Au(III). *HETEROCYCLES* 25, 297 (1987).

14. Mizushima, E., Hayashi, T. & Tanaka, M. Au(I)-Catalyzed Highly Efficient Intermolecular Hydroamination of Alkynes. *Org. Lett.* **5**, 3349–3352 (2003).

15. Rudolph, M. & Hashmi, A. S. K. Heterocycles from Gold Catalysis. *Chem. Commun.* **47**, 6536–6544 (2011).

16. Santhoshkumar, R., Cheng, C.-H. Reaching Green: Heterocycle Synthesis by Transition Metal-Catalyzed C-H Functionalization in Sustainable Medium. Chemistry – A European Journal **25**, 9366-9384 (2019).

17. Royer J. Asymmetric Synthesis of Nitrogen Heterocycles (Wiley-VCH, 2009).

18. Xi, M. & Bent, B. E. Mechanisms of the Ullmann Coupling Reaction in Adsorbed Monolayers. *J. Am. Chem. Soc.* 115, 7426–7433 (1993).

19. Held, P. A., Gao, H.-Y., Liu, L., Mück-Lichtenfeld, C., Timmer, A., Mönig, H., Barton, D., Neugebauer, J., Fuchs, H. & Studer, A. On-Surface Domino Reactions: Glaser Coupling and Dehydrogenative Coupling of a Biscarboxylic Acid To Form Polymeric Bisacylperoxides. *Angewandte Chemie International Edition* **55**, 9777–9782 (2016).

20. Kanuru, V. K., Kyriakou, G., Beaumont, S. K., Papageorgiou, A. C., Watson, D. J. & Lambert, R. M. Sonogashira Coupling on an Extended Gold Surface in Vacuo: Reaction of Phenylacetylene with Iodobenzene on Au(111). *J. Am. Chem. Soc.* **132**, 8081–8086 (2010).

21. Cai, J., Ruffieux, P., Jaafar, R., Bieri, M., Braun, T., Blankenburg, S., Muoth, M., Seitsonen, A. P., Saleh, M., Feng, X., Müllen, K. & Fasel, R. Atomically precise bottom-up fabrication of graphene nanoribbons. *Nature* **466**, 470–473 (2010).

22. Clair, S. & de Oteyza, D. G. Controlling a chemical coupling reaction on a surface: tools and strategies for on-surface synthesis. *Chemical reviews* **119**, 4717-4776 (2019).

23. de Oteyza, D. G., Gorman, P., Chen, Y. C., Wickenburg, S., Riss, A., Mowbray, D. J., Etkin, G., Pedramrazi, Z., Tsai, H.-Z., Rubio, A., Crommie, M. F. & Fischer, F. R. Direct imaging of covalent bond structure in single-molecule chemical reactions. *Science* **340**, 1434-1437 (2013).

24. Morgenstern, K. Isomerization reactions on single adsorbed molecules. Accounts of chemical research **42**, 213-223 (2009).

25. Kaiser, K., Scriven, L. M., Schulz, F., Gawel, P., Gross, L. & Anderson, H. L. An Sp-Hybridized Molecular Carbon Allotrope, Cyclo[18]Carbon. *Science* **365**, 1299–1301 (2019).

26. Mallada, B., de la Torre, B., Mendieta-Moreno, J. I., Nachtigallová, D., Matěj, A., Matoušek, M., Mutombo, P., Brabec, J., Veis, L., Cadart, T., Kotora, M. & Jelínek, P. On-Surface Strain-Driven Synthesis of Nonalternant Non-Benzenoid Aromatic Compounds Containing Four- to Eight-Membered Rings. *J. Am. Chem. Soc.* **143**, 14694–14702 (2021).

27. Zhong, Q., Hu, Y., Niu, K., Zhang, H., Yang, B., Ebeling, D., Tschakert, J., Cheng, T., Schirmeisen, A., Narita, A., Müllen, K. & Chi, L. Benzo-Fused Periacenes or Double Helicenes? Different Cyclodehydrogenation Pathways on Surface and in Solution. *J. Am. Chem. Soc.* **141**, 7399–7406 (2019).

28. Mendieta-Moreno, J. I., Mallada, B., de la Torre, B., Cadart, T., Kotora, M. & Jelínek, P. Unusual Scaffold Rearrangement in Polyaromatic Hydrocarbons Driven by Concerted Action of Single Gold Atoms on a Gold Surface. *Angewandte Chemie International Edition* **61**, e202208010 (2022).

29. Gross, L., Mohn, F., Moll, N., Liljeroth, P. & Meyer, G. The Chemical Structure of a Molecule Resolved by Atomic Force Microscopy. *Science* **325**, 1110–1114 (2009).

30. Pascal, S. & Siri, O. Benzoquinonediimine Ligands: Synthesis, Coordination Chemistry and Properties. *Coordination Chemistry Reviews* **350**, 178–195 (2017).

31. Siri, O., Braunstein, P., Rohmer, M.-M., Bénard, M. & Welter, R. Novel "Potentially Antiaromatic", Acidichromic Quinonediimines with Tunable Delocalization of Their 6π-Electron Subunits. *J. Am. Chem. Soc.* **125**, 13793–13803 (2003).

32. Dähne, S. & Leupold, D. Coupling Principles in Organic Dyes. *Angewandte Chemie International Edition in English* **5**, 984–993 (1966).

33. Ye, D., Wang, J., Zhang, X., Zhou, Y., Ding, X., Feng, E., Sun, H., Liu, G., Jiang, H. & Liu, H. Gold-Catalyzed Intramolecular Hydroamination of Terminal Alkynes in Aqueous Media: Efficient and Regioselective Synthesis of Indole-1-Carboxamides. *Green Chemistry* **11**, 1201–1208 (2009).

34. Heckershoff, R., Maier, S., Wurm, T., Biegger, P., Brödner, K., Krämer, P., Hoffmann, M. T., Eberle, L., Stein, J., Rominger, F., Rudolph, M., Freudenberg, J., Dreuw, A., Hashmi, A. S. K. & Bunz, U. H. F. Cyclopentannulated Dihydrotetraazapentacenes. *Chemistry – A European Journal* **28**, e202104203 (2022).

35. Collective Diffusion on Surfaces: Correlation Effects and Adatom Interactions: Proceedings of the NATO Advanced Research Workshop on Collective Diffusion on Surfaces: Correlation Effects and Adatom Interactions Prague, Czech Republic 2–6 October 2000, Tringides, M. C., Chvoj, Z., Eds.; NATO Science Series II: Mathematics, Physics and Chemistry; Springer Netherlands: Dordrecht, Vol. 29 (2021).

36. *Surface Diffusion: Atomistic and Collective Processes*, Tringides, M. C., Ed.; NATO ASI Series; Springer US: Boston, MA, Vol. 360 (1997).

37. Björk, J., Sánchez-Sánchez, C., Chen, Q., Pignedoli, C. A., Rosen, J., Ruffieux, P., Feng, X., Narita, A., Müllen, K. & Fasel, R. The Role of Metal Adatoms in a Surface-Assisted Cyclodehydrogenation Reaction on a Gold Surface. *Angewandte Chemie International Edition* **61**, e202212354 (2022).

38. Zhang, Z., Perepichka, D. F. & Khaliullin, R. Z. Adatoms in the Surface-Confined Ullmann Coupling of Phenyl Groups. *J. Phys. Chem. Lett.* **12**, 11061–11069 (2021).

39. Jiménez-Martín, A., Villalobos, F., Mallada, B., Edalatmanesh, S., Matěj, A., M. Cuerva, J., Jelínek, P., G. Campaña, A. & de la Torre, B. On-Surface Synthesis of Non-Benzenoid Conjugated Polymers by Selective Atomic Rearrangement of Ethynylarenes. *Chemical Science* **14**, 1403–1412 (2023).

40. Niu, K., Lin, H., Zhang, J., Zhang, H., Li, Y., Li, Q. & Chi, L. Mechanistic Investigations of the Au Catalysed C–H Bond Activations in on-Surface Synthesis. *Phys. Chem. Chem. Phys.* **20**, 15901–15906 (2018).

41. Wang, Y., Wang, Z., Li, Y., Wu, G., Cao, Z. & Zhang, L. A General Ligand Design for Gold Catalysis Allowing Ligand-Directed Anti-Nucleophilic Attack of Alkynes. *Nat Commun* **5**, 3470 (2014).

42. Sohel, S. M. A. & Liu, R.-S. Carbocyclisation of Alkynes with External Nucleophiles Catalysed by Gold, Platinum and Other Electrophilic Metals. *Chem. Soc. Rev.* **38**, 2269–2281 (2009).

43. Gao, H.-Y., Wagner, H., Zhong, D., Franke, J.-H., Studer, A. & Fuchs, H. Glaser Coupling at Metal Surfaces. *Angewandte Chemie International Edition* **52**, 4024–4028 (2013).

44. Saywell, A., Browning, A. S., Rahe, P., Anderson, H. L. & Beton, P. H. Organisation and Ordering of 1D Porphyrin Polymers Synthesised by On-Surface Glaser Coupling. *Chem. Commun.* **52**, 10342–10345 (2016).

45. Zhang, Y.-Q., Kepčija, N., Kleinschrodt, M., Diller, K., Fischer, S., Papageorgiou, A. C., Allegretti, F., Björk, J., Klyatskaya, S., Klappenberger, F., Ruben, M. & Barth, J. V. Homo-Coupling of Terminal Alkynes on a Noble Metal Surface. *Nat Commun* **3**, 1286 (2012).

46. Müller, T. E., Grosche, M., Herdtweck, E., Pleier, A.-K., Walter, E. & Yan, Y.-K. Developing Transition-Metal Catalysts for the Intramolecular Hydroamination of Alkynes. *Organometallics* **19**, 170–183 (2000).

47. Pohlki, F. & Doye, S. The Catalytic Hydroamination of Alkynes. *Chem. Soc. Rev.* **32**, 104–114 (2003).

48. Severin, R. & Doye, S. The Catalytic Hydroamination of Alkynes. *Chem. Soc. Rev.* **36**, 1407–1420 (2007).

49. Giessibl, F. J. The qPlus Sensor, a Powerful Core for the Atomic Force Microscope. *Review of Scientific Instruments* **90**, 011101 (2019).

50. Horcas, I., Fernández, R., Gómez-Rodríguez, J. M., Colchero, J., Gómez-Herrero, J. & Baro, A. M. WSXM: A Software for Scanning Probe Microscopy and a Tool for Nanotechnology. *Review of Scientific Instruments* **78**, 013705 (2007).

51. Mendieta-Moreno, J. I., Walker, R. C., Lewis, J. P., Gómez-Puertas, P., Mendieta, J. & Ortega, J. Fireball/Amber: An Efficient Local-Orbital DFT QM/MM Method for Biomolecular Systems. *J. Chem. Theory Comput.* **10**, 2185–2193 (2014).

52. Lewis, J. P., Jelínek, P., Ortega, J., Demkov, A. A., Trabada, D. G., Haycock, B., Wang, H., Adams, G., Tomfohr, J. K., Abad, E., Wang, H. & Drabold, D. A. Advances and Applications in the FIREBALL Ab Initio Tight-Binding Molecular-Dynamics Formalism. *physica status solidi (b)* **248**, 1989–2007 (2011).

53. Pearlman, D. A., Case, D. A., Caldwell, J. W., Ross, W. S., Cheatham, T. E., DeBolt, S., Ferguson, D., Seibel, G. & Kollman, P. AMBER, a Package of Computer Programs for Applying Molecular Mechanics, Normal Mode Analysis, Molecular Dynamics and Free Energy Calculations to Simulate the Structural and Energetic Properties of Molecules. *Computer Physics Communications* **91**, 1–41 (1995).

54. Case, D. A., Cheatham III, T. E., Darden, T., Gohlke, H., Luo, R., Merz Jr., K. M., Onufriev, A., Simmerling, C., Wang, B. & Woods, R. J. The Amber Biomolecular Simulation Programs. *Journal of Computational Chemistry* **26**, 1668–1688 (2005).

55. Darve, E. & Pohorille, A. Calculating Free Energies Using Average Force. *The Journal of Chemical Physics* **115**, 9169–9183 (2001).

56. Izrailev, S., Stepaniants, S., Isralewitz, B., Kosztin, D., Lu, H., Molnar, F., Wriggers, W. & Schulten, K. Steered Molecular Dynamics. In *Computational Molecular Dynamics: Challenges, Methods, Ideas*; Deuflhard, P., Hermans, J., Leimkuhler, B., Mark, A. E., Reich, S., Skeel, R. D., Eds.; Lecture Notes in Computational Science and Engineering; Springer: Berlin, Heidelberg, pp 39–65 (1999).

57. Pastor, R. W.; Brooks, B. R.; Szabo, A. An Analysis of the Accuracy of Langevin and Molecular Dynamics Algorithms. *Molecular Physics* **65**, 1409–1419 (1988).

58. Kumar, S., Rosenberg, J. M., Bouzida, D., Swendsen, R. H. & Kollman, P. A. THE Weighted Histogram Analysis Method for Free-Energy Calculations on Biomolecules. I. The Method. *Journal of Computational Chemistry* **13**, 1011–1021 (1992).

59. Blum, V., Gehrke, R., Hanke, F., Havu, P., Havu, V., Ren, X., Reuter, K. & Scheffler, M. Ab Initio Molecular Simulations with Numeric Atom-Centered Orbitals. *Computer Physics Communications* **180**, 2175–2196 (2009).

60. Becke, A. D. Density-functional Thermochemistry. I. The Effect of the Exchange-only Gradient Correction. *The Journal of Chemical Physics* **96**, 2155–2160 (1992).

61. Stephens, P. J., Devlin, F. J., Chabalowski, C. F. & Frisch, M. J. Ab Initio Calculation of Vibrational Absorption and Circular Dichroism Spectra Using Density Functional Force Fields. *J. Phys. Chem.* **98**, 11623–11627 (1994).

62. Tkatchenko, A. & Scheffler, M. Accurate Molecular Van Der Waals Interactions from Ground-State Electron Density and Free-Atom Reference Data. *Phys. Rev. Lett.* **102**, 073005 (2009).

63. Hapala, P., Temirov, R., Tautz, F. S. & Jelínek, P. Origin of High-Resolution IETS-STM Images of Organic Molecules with Functionalized Tips. *Phys. Rev. Lett.* **113**, 226101 (2014).

64. Hapala, P., Kichin, G., Wagner, C., Tautz, F. S., Temirov, R. & Jelínek, P. Mechanism of High-Resolution STM/AFM Imaging with Functionalized Tips. *Phys. Rev. B* **90**, 085421 (2014).

65. Krejčí, O., Hapala, P., Ondráček, M. & Jelínek, P. Principles and Simulations of High-Resolution STM Imaging with a Flexible Tip Apex. *Phys. Rev. B* **95**, 045407 (2017).

Scheme

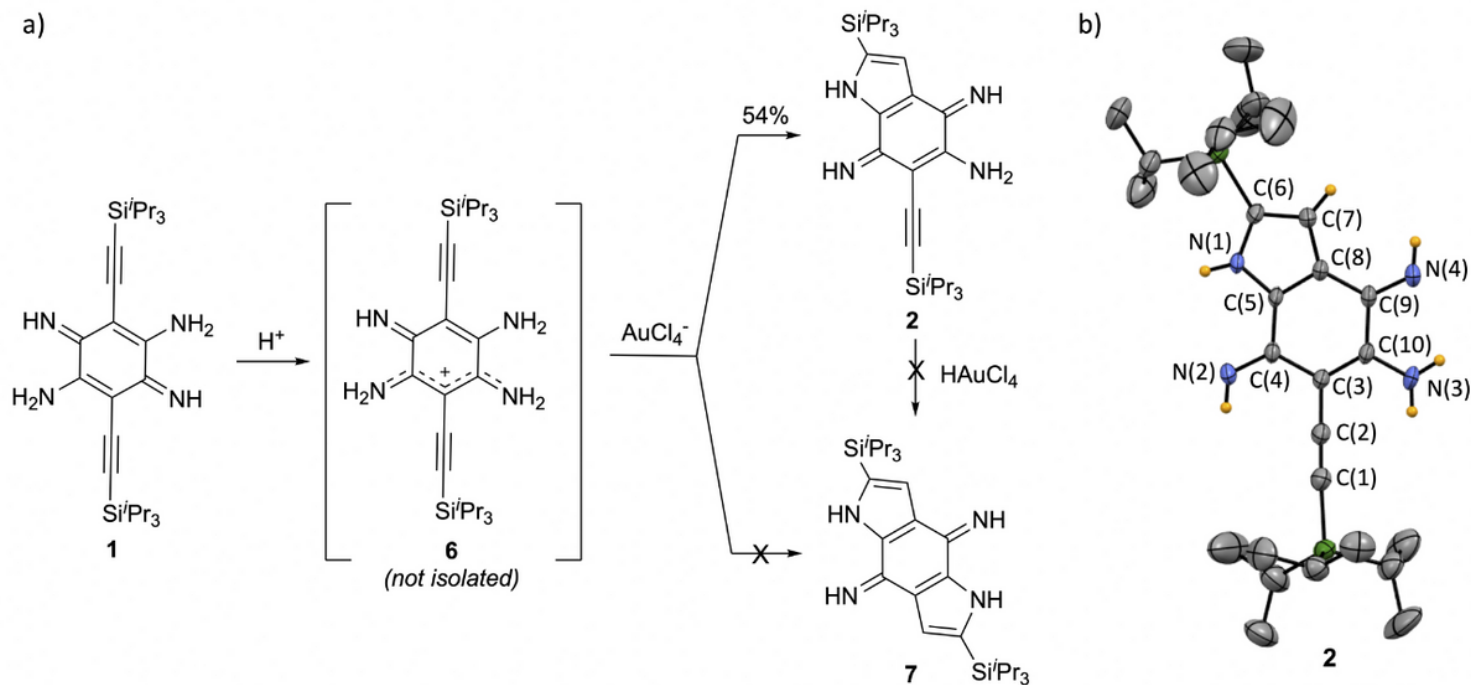Scheme 1 is available in the Supplementary Files section.

Figures

Figure 1

In-solution synthesis of 2. a) Proposed formation of **2** via the protonation of **1** into intermediate **6**, followed by AuCl$_4^-$ catalyzed N-cyclization. The figure shows the non-formation of product **7** with AuCl$_4$-nor via second ring cyclization from **2** in the presence of HAuCl$_4$- b) ORTEP view of **2**. Ellipsoid plots at 50 % probability level. Bond lengths (Å): C(1)-C(2) = 1.185, C(2)-C(3) = 1.431, C(3)-C(4) = 1.466, C(4)-C(5) = 1.453, C(5)-N(1) = 1.356, N(1)-C(6) = 1.378, C(6)-C(7) = 1.394, C(7)-C(8) = 1.412, C(8)-C(9) = 1.445, C(9)-C(10) = 1.489, C(10)-C(3) = 1.378, C(5)-C(8) = 1.377, C(4)-N(2) = 1.287, C(9)-N(4) = 1.282, C(10)-N(3) = 1.346.
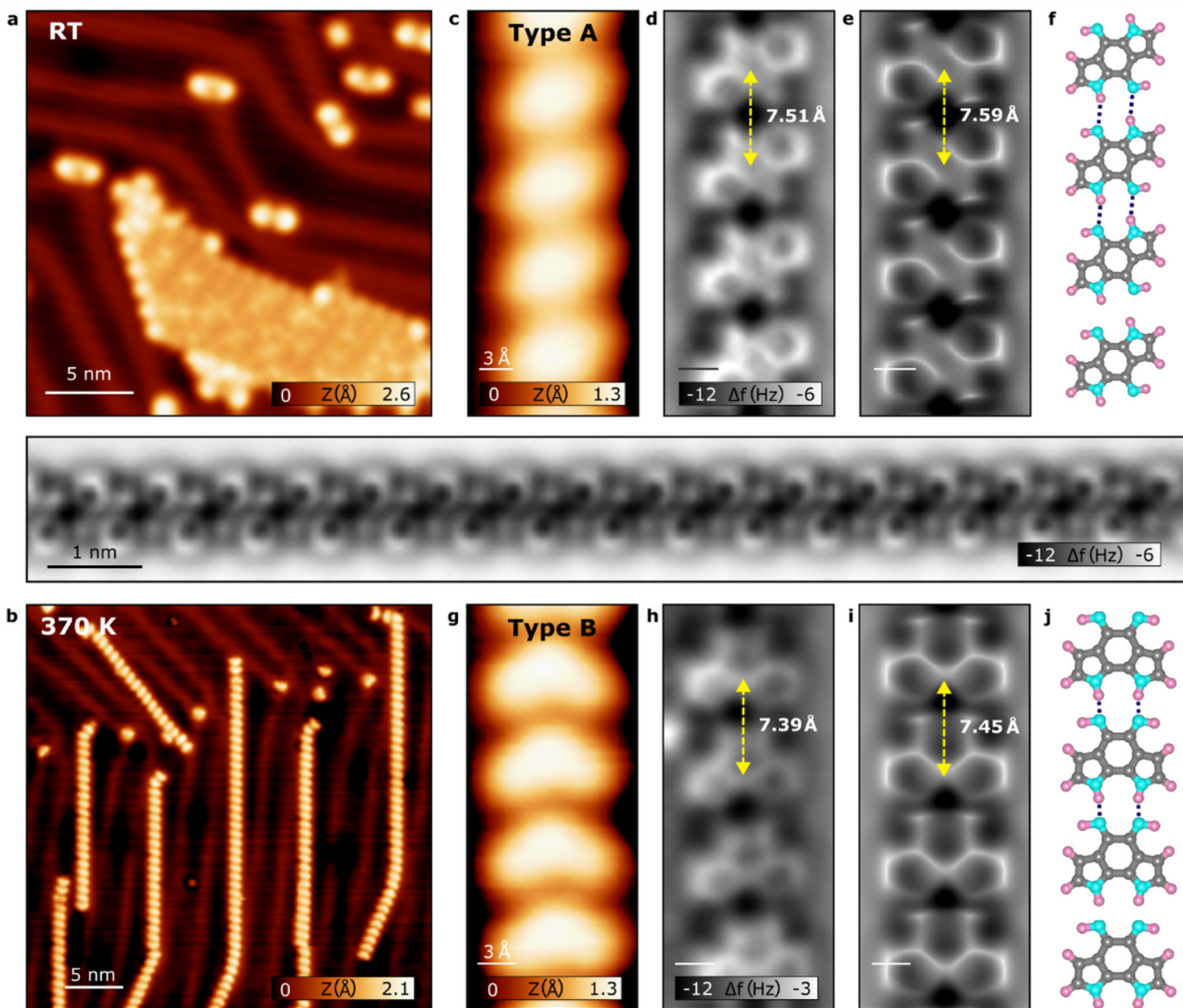
Figure 2

On-surface characterization of compounds 4 and 5. a) STM topographic overview after deposition at RT of the molecular precursor **3** (-1 V, 10 pA). b) STM topographic overview after annealing the sample at 370 K (0.1 V, 10 pA). Type A c) STM topographic close-up image (1 V, 5 pA), d) experimental nc-AFM detailed image, e) simulated nc-AFM image and f) molecular model (in grey (C), blue (N) and pink (H)) of final product **4**. Type B g) STM topographic close-up image (50 mV, 10 pA), h) experimental nc-AFM detailed image, i) simulated nc-AFM image and j) molecular model of final product **5**.
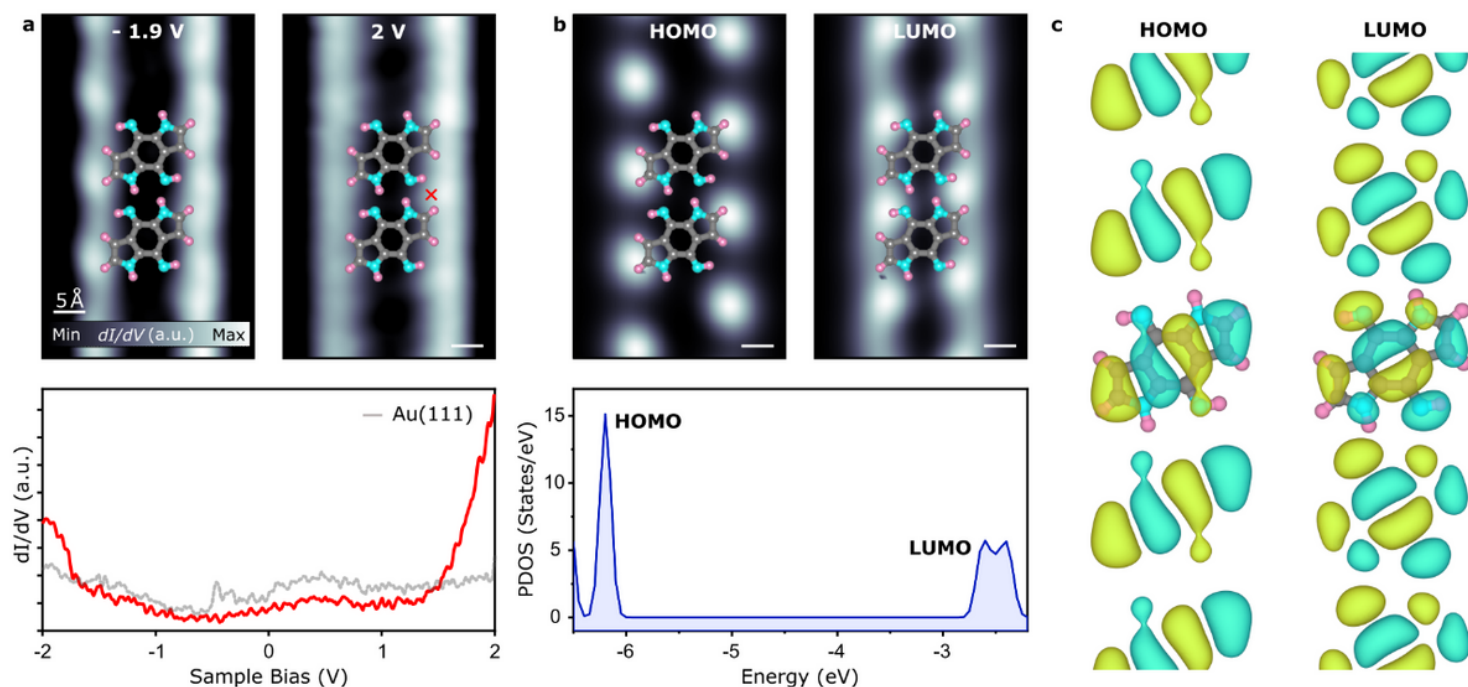
Figure 3

Electronic characterization of final product 4. a) Experimental constant-current *dI/dV* maps at -1.9 V (left) and 2 V (right) of final product **4** with the corresponding conductance spectra. b) Calculated PDOS of the HOMO (left) and LUMO (right) with the DFT calculated LDOS for structure **4**. c) Canonical DFT orbitals of HOMO and LUMO of **4**.
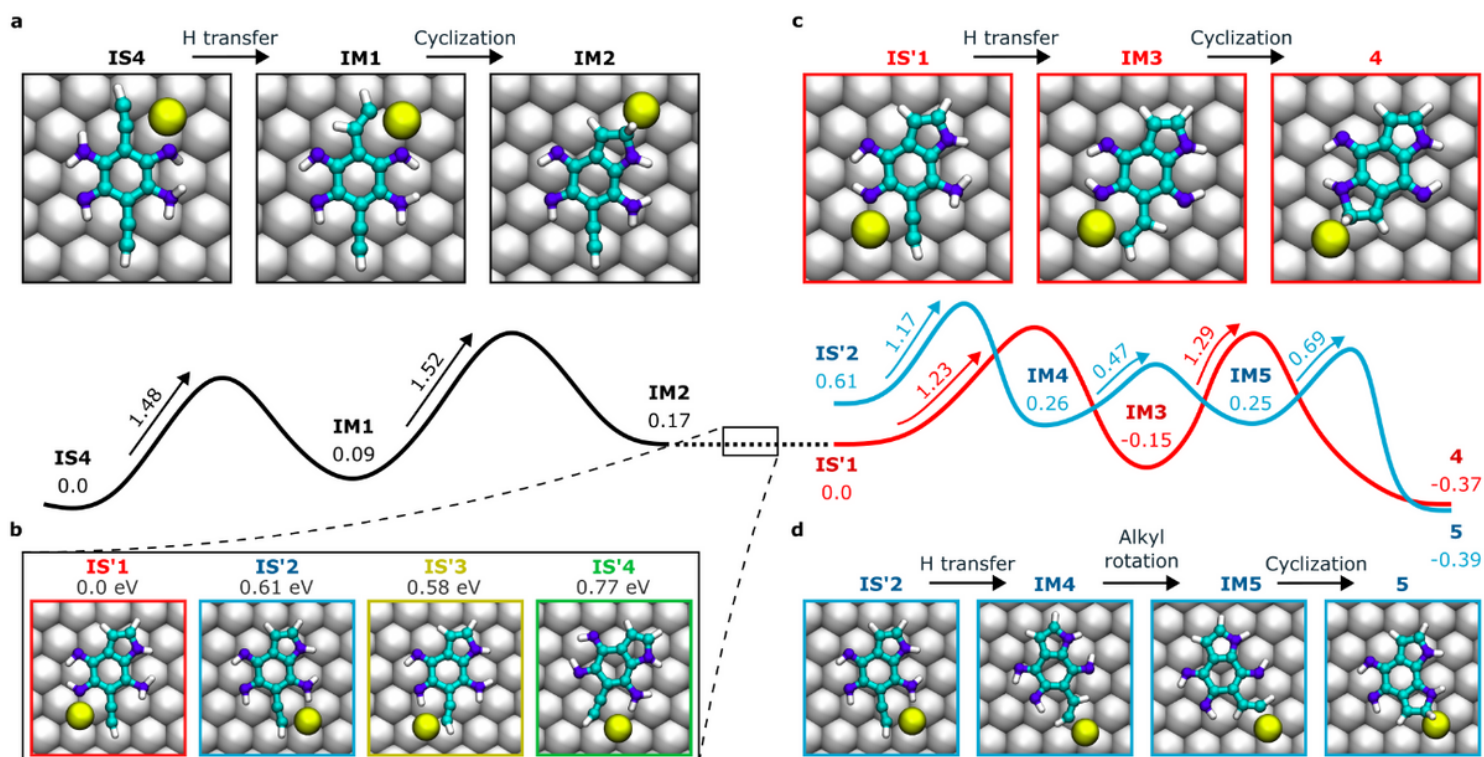

Figure 4

Free-energy calculations of surface-catalyzed reaction pathways. a) Simulated snapshots and activation energies of the reaction steps from the initial state **4** (**IS4**), intermediate state **1** (**IM1**) and intermediate state **2** (**IM2**) of the first ring cyclization. b) Energy comparison and simulated molecular positions between the initial states (**IS's**) for the second ring cyclization reaction. c) Top-view reaction snapshots and free energy profile (red) for the initial state (**IS'1**), intermediate state (**IM3**) and the final product (**4**) of the second ring cyclization for **4**. d) Simulated images and energy reaction pathway (blue) for the initial state (**IS'2**), intermediate state **4** (**IM4**), intermediate state **5** (**IM5**) and the final product state (**5**) of the second ring closure for **5**. Energies are presented in eV.

Supplementary Files

This is a list of supplementary files associated with this preprint. Click to download.

- Scheme1.png
- JimenezMartinSI.docx